

A modified X-ray diffraction method to measure residual normal and shear stresses of machined surfaces

LUO, Quanshun <<http://orcid.org/0000-0003-4102-2129>>

Available from Sheffield Hallam University Research Archive (SHURA) at:

<https://shura.shu.ac.uk/29495/>

This document is the Published Version [VoR]

Citation:

LUO, Quanshun (2022). A modified X-ray diffraction method to measure residual normal and shear stresses of machined surfaces. *International Journal of Advanced Manufacturing Technology*, 119 (5-6), 3595-3606. [Article]

Copyright and re-use policy

See <http://shura.shu.ac.uk/information.html>



A modified X-ray diffraction method to measure residual normal and shear stresses of machined surfaces

Quanshun Luo¹

Received: 15 September 2021 / Accepted: 28 December 2021
© The Author(s) 2022

Abstract

X-ray diffraction has been widely used in measuring surface residual stresses. A drawback of the conventional $d \sim \sin^2\psi$ method is the increased uncertainty arising from $\sin^2\psi$ splitting when a significant residual shear stress co-exists with a residual normal stress. In particular, the conventional method can only be applied to measure the residual normal stress while leaving the residual shear stress unknown. In this paper, we propose a new approach to make simultaneous measurement of both residual normal and shear stresses. Theoretical development of the new approach is described in detail, which includes two linear regressions, $\frac{d_{\psi+d_{-\psi}}}{2} \sim \sin^2\psi$ and $\{d_{\psi}-d_{-\psi}\} \sim \sin(2\psi)$, to determine the residual normal and shear stresses separately. Several samples were employed to demonstrate the new method, including turning-machined and grinding-machined cylindrical bars of a high strength steel as well as a flat sample of magnetron sputtered TiN coating. The machined samples were determined to have residual compressive normal stresses at both the axial and hoop directions as well as various scales of residual shear stresses. The TiN coating showed a high scale of residual compressive (normal) stress whereas the measured residual shear stress was extremely low. The new method showed significantly increased precision as compared to the conventional $d \sim \sin^2\psi$ method.

Keywords Residual stress measurement · X-ray diffraction · Machined surfaces · Residual shear stresses · Residual normal stresses

1 Introduction

X-ray diffraction (XRD) is a powerful analytical tool in characterising polycrystalline materials owing to its accurate measurement of lattice d-spacings. An important application has been the quantitative determination of surface residual stresses, in which $d \sim \sin^2\psi$ linear regression is the mostly used method [1–8]. The conventional $d \sim \sin^2\psi$ method is suitable for measuring in-plane normal stresses (i.e., zero normal stress vertical to the measured surface) if the related residual shear stresses can be ignored. In such circumstances, the d-spacings measured at a series of off-axis angle ψ , d_{ψ} , are correlated to $\sin^2\psi$ with small data scattering. This method has been widely used in determining the residual normal stresses of thin films and coatings as well as various mechanically strengthened surfaces [1, 2, 5–7, 9, 10].

However, applications of the $d \sim \sin^2\psi$ method become problematic in analysing surfaces where residual shear stresses co-exist with residual normal stresses. A common feature arising from such measurements is the so-called $\sin^2\psi$ splitting, i.e., different slopes of $d \sim \sin^2\psi$ linear regression between positive and negative ψ values [3, 11, 12].

The co-existence of residual normal and shear stresses appears in most machined surfaces. In machining, the edge of a cutting tool provides combined compressive and shear loads to a small volume in front of the cutting edge. Meanwhile, its flank surface keeps frictional contact to the machined surface under compressive and shear loads. These loads generate non-homogeneous plastic deformation in certain depth of the machined surface and consequently result in the formation of residual stresses. In addition, the deformation and friction also induce rapid heating and subsequent cooling of the machined surface in certain depth, which also contributes to the residual stresses. Residual stresses resulting from grinding, turning, and milling have been studied extensively [8, 11–25]. For example, Xin and Zhang reported residual tensile stresses of high strength

✉ Quanshun Luo
q.luo@shu.ac.uk

¹ Materials and Engineering Research Institute, Sheffield Hallam University, Sheffield S1 1WB, UK

steels after turning or high speed milling [13, 14]. For ultra-high strength steels and other high strength materials, the prevention of residual tensile stresses is critical because such stresses cause certain loss of fatigue resistance [13, 15, 22]. It has been reported that, machining-induced surface residual stresses greatly affect the fatigue properties of high strength metallic alloys, whereas shot peening and other types of surface strengthening processes produce residual compressive stresses [26–28]. Moreover, residual stresses existing in welds and forgings have been found to trigger fatigue fracture and or corrosion cracking [29–35].

Quantitative measurement of residual normal and shear stresses is highly demanded, especially those stresses existing in machined surfaces. Studies of residual shear stresses have been reported in several publications. Perenda and co-authors reported the generation of residual normal and shear stresses in pre-setting and deep rolling treated high strength steel torsion bars [22]. Meixner and co-authors studied the near-surface stresses of ground and peened high strength steels [8]. Zauskova et al. examined the three-dimensional residual normal and shear stresses by employing the $d \sim \sin^2\psi$ method at three sample orientations [24]. These examples suggest that the measurement of residual shear stress has drawn the attention of researchers in recent years. In practice, the conventional $d \sim \sin^2\psi$ method shows drawbacks such as low precision arising from the $\sin^2\psi$ splitting. In addition, this method is limited to the measurement of residual normal stresses only, because of the theoretical difficulty in measuring combined normal and shear stresses. To overcome the drawbacks, some researchers recommended non-linear $d \sim \sin^2\psi$ regression or the use of 3-dimensional measurement, which normally required large sum of experimental measurements and subsequent calculation [11]. In addition to these, an alternative XRD $\cos\alpha$ method has been introduced in recent research [23, 36]. Comparing to the traditional $\sin^2\psi$ method, the $\cos\alpha$ method can measure both normal and shear stresses simultaneously and requires shorter experiment time. These advantages are attributed

to the special instrumental settings of the $\cos\alpha$ method that it employs a 2-dimensional detector to detect the whole Debye–Scherrer ring in a single measurement.

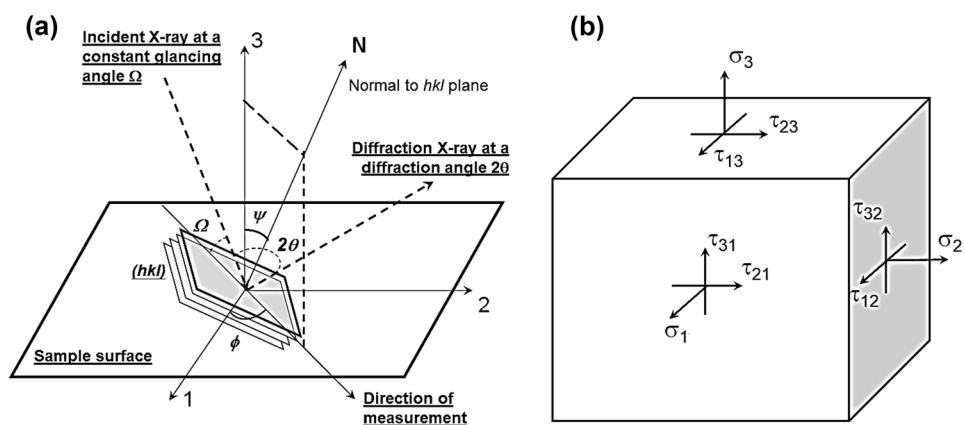
In this paper, we present a new approach of XRD residual stress measurement through a modification to the conventional $d \sim \sin^2\psi$ method. The modification includes a careful pre-setting of incident angles, Ω , to obtain a series of off-axis angles, $\pm\psi$, followed by two linear regressions developed from the conventional $d \sim \sin^2\psi$ linear regression. Several machined surfaces, as well as a magnetron sputtered hard coating, were employed to demonstrate the new approach and to verify its reliability and accuracy. It has been demonstrated that the new technique can be applied to make simultaneous measurement of residual normal and shear stresses. The advantages of the new approach include the significantly improved precision in measuring residual normal stresses and, more importantly, a method to measure the accompanying residual shear stresses. In the following sections, we will first describe the new analytical solution by developing two modified linear regressions. Then, a procedure of detailed XRD experiments will be provided, followed by the measurements on a few machined steel bars.

2 Theoretical development of new equations

2.1 General theoretical approach

Figure 1a illustrates schematically the configuration of XRD $d \sim \sin^2\psi$ method of a polycrystalline solid. A beam of single-wavelength X-ray hits the surface at an incident angle Ω and gives rise to a diffraction beam of a specific crystal-line lattice plane (hkl) at a diffraction angle 2θ . The vector N , which has an off-axis angle ψ with respect to Axis 3, is the normal of the (hkl) plane. The vectors of the incident X-ray, diffraction X-ray, N and Axis 3 are in the same plane. The geometric projection of N to the sample surface, which

Fig. 1 Schematic charts of **a** definition of the three reference axes and the direction of XRD stress measurement; and **b** the normal and shear stresses in the 3-dimensional system



defines the direction of the stress to be measured, forms an angle ϕ with respect to Axis 1. The three angles ψ , Ω and 2θ obey the relationship $\psi + \Omega = \theta$. Therefore, the off-axis angle ψ can be determined from the measured diffraction angle 2θ . Meanwhile, the 2θ angle also determines the d-spacing d_ψ of the (hkl) plane using the Bragg law $d_\psi = \frac{\lambda}{2 \cdot \sin\theta}$, where λ stands for the X-ray wavelength.

Figure 1b presents the nine stress vectors of the system, in which σ and τ stand for normal stresses and shear stresses, respectively. Equation (1) is the fundamental equation of XRD residual stress measurement, in which the residual strain in the (hkl) plane being calculated from the XRD measured d-spacing ($d_{\phi\psi}$) and the strain-free d-spacing (d_0) is expressed as a complex function of several factors, including the elastic modulus (E) and Poisson's ratio (ν) of the crystalline solid, the geometric factors ψ and ϕ , and the stresses σ and τ [11, 12]. An in-plane stress state is assumed for surface residual stress measurement, i.e., $\sigma_3 = 0$. Consequently, Eq. (1) is re-written as Eq. (2). By defining $\phi = 0$, i.e., considering the measurement following Axis-1, Eq. (2) is re-written as Eq. (3), and then Eq. (4).

Equation (4) is the principal formula for XRD residual stress measurement. The linear relationship between d_ψ and $\sin^2\psi$ exists only when the system is free from residual shear stress, i.e., $\tau_{13} = 0$.

$$\frac{d_{\phi\psi} - d_0}{d_0} = \frac{1 + \nu}{E} \cdot (\sigma_1 \cdot \cos^2\phi + \tau_{12} \cdot \sin 2\phi + \sigma_2 \cdot \sin^2\phi - \sigma_3) \cdot \sin^2\psi + \frac{1 + \nu}{E} \cdot \sigma_3 - \frac{\nu}{E} \cdot (\sigma_1 + \sigma_2 + \sigma_3) + \frac{1 + \nu}{E} \cdot (\tau_{13} \cdot \cos\phi + \tau_{23} \cdot \sin\phi) \cdot \sin(2\psi) \tag{1}$$

$$\frac{d_{\phi\psi} - d_0}{d_0} = \frac{1 + \nu}{E} \cdot (\sigma_1 \cdot \cos^2\phi + \tau_{12} \cdot \sin 2\phi + \sigma_2 \cdot \sin^2\phi) \cdot \sin^2\psi - \frac{\nu}{E} \cdot (\sigma_1 + \sigma_2) + \frac{1 + \nu}{E} \cdot (\tau_{13} \cdot \cos\phi + \tau_{23} \cdot \sin\phi) \cdot \sin(2\psi) \tag{2}$$

$$\frac{d_\psi - d_0}{d_0} = \frac{1 + \nu}{E} \cdot \sigma_1 \cdot \sin^2\psi + \frac{1 + \nu}{E} \cdot \tau_{13} \cdot \sin(2 \cdot \psi) - \frac{\nu}{E} \cdot (\sigma_1 + \sigma_2) \tag{3}$$

$$d_\psi = \frac{1 + \nu}{E} \cdot \sigma_1 \cdot d_0 \cdot \sin^2\psi + \frac{1 + \nu}{E} \cdot \tau_{13} \cdot d_0 \cdot \sin(2 \cdot \psi) - \frac{\nu}{E} \cdot d_0 \cdot (\sigma_1 + \sigma_2) + d_0 \tag{4}$$

2.2 Conventional approach to measure residual normal stress

The conventional approach is made by assuming a shear-stress-free system. Consequently, Eq. (4) is converted to Eq. (5) which facilitates a linear regression between d_ψ and $\sin^2\psi$. This approach has been widely adopted in measuring residual

stresses of thin films and coatings [1–8]. The solution of the linear regression is provided in Eq. (6), including the definition of the two constants A and B. In most cases, the values of residual stresses are much smaller than the elastic modulus E. Consequently, Eq. (7) is derived to calculate the values of σ_1 and d_0 , respectively, after assuming a uniaxial in-plane stress ($\sigma_1 = \sigma_2$) condition.

$$d_\psi = \frac{1 + \nu}{E} \cdot \sigma_1 \cdot d_0 \cdot \sin^2\psi - \frac{\nu}{E} \cdot d_0 \cdot (\sigma_1 + \sigma_2) + d_0 \tag{5}$$

$$d_\psi = A \cdot \sin^2\psi + B; A = \frac{1 + \nu}{E} \cdot \sigma_1 \cdot d_0; B = d_0 \cdot (1 - \nu) \cdot \frac{\sigma_1 + \sigma_2}{E} \tag{6}$$

$$\sigma_1 = \frac{A \cdot E}{2 \cdot \nu \cdot A + (1 + \nu) \cdot B}; d_0 = \frac{2 \cdot \nu}{1 + \nu} \cdot A + B \tag{7}$$

2.3 New approach to measure both residual normal and shear stresses

In this paper, we propose an approach to determine both the residual normal stress and residual shear stress. In experiment, it is feasible to acquire diffraction peaks of the selected lattice plane (hkl) at a series of plus and minus off-axis angles $\{\psi, -\psi\}_i$ for $i = 1, 2, \dots, n$ (e.g., $n = 5$ in this

paper). For a pair of positive ψ and negative $-\psi$, we convert Eq. (4) to Eq. (8) by replacing ψ with its negative value $-\psi$. After that, Eqs. (9)–(14) are produced through simple treatments of Eqs. (4) and (8). These form new linear regressions for the determination of σ_1 and τ_{13} , respectively. Equation (9) suggests a linear relationship between $\sin^2\psi$ and $\frac{d_\psi + d_{-\psi}}{2}$, seeing details of the expressions in Eq. (10). Following the linear plotting, the residual normal stress σ_1 and the strain-free d-spacing d_0 are obtained in Eq. (11). Equations (12) and (13) set up a linear relationship between $(d_\psi - d_{-\psi})$ and $\sin(2\psi)$. Then, the residual shear stress is obtained after constant C is derived from the linear regression, Eq. (14).

The new approach is termed as the $\sin^2\psi$ - $\sin(2\psi)$ method to differentiate it from the conventional $d \sim \sin^2\psi$ method.

$$d_{-\psi} = \frac{1 + \nu}{E} \cdot \sigma_1 \cdot d_0 \cdot \sin^2(-\psi) + \frac{1 + \nu}{E} \cdot \tau_{13} \cdot d_0 \cdot \sin(-2\psi) - \frac{\nu}{E} \cdot d_0 \cdot (\sigma_1 + \sigma_2) + d_0 \tag{8}$$

$$\frac{d_\psi + d_{-\psi}}{2} = \frac{1 + \nu}{E} \cdot \sigma_1 \cdot d_0 \cdot \sin^2\psi - \frac{\nu}{E} \cdot d_0 \cdot (\sigma_1 + \sigma_2) + d_0 \tag{9}$$

$$\frac{d1_{\psi} + d1_{-\psi}}{2} = A \cdot \sin^2\psi + B; A = \frac{1 + \nu}{E} \cdot \sigma_1 \cdot d_0; B = d_0 - \frac{\nu}{E} \cdot d_0 \cdot (\sigma_1 + \sigma_2) \tag{10}$$

$$\sigma_1 = \frac{A \cdot E}{2 \cdot \nu \cdot A + (1 + \nu) \cdot B}; d_0 = \frac{2 \cdot \nu}{1 + \nu} \cdot A + B \tag{11}$$

$$d_{\psi} - d_{-\psi} = 2 \frac{1 + \nu}{E} \cdot \tau_{13} \cdot d_0 \cdot \sin(2\psi) \tag{12}$$

$$d_{\psi} - d_{-\psi} = C \cdot \sin(2\psi) + D; C = 2 \cdot \frac{1 + \nu}{E} \cdot \tau_{13} \cdot d_0; D = 0 \tag{13}$$

$$\tau_{13} = \frac{C \cdot E}{2 \cdot d_0 \cdot (1 + \nu)} \tag{14}$$

3 Experimental details

Several samples were employed to demonstrate the new approach, including machined cylindrical tensile bars, of 5 mm in diameter, of a high-strength spring steel as well as a TiN coating. The spring steel was strengthened through quenching and tempering heat treatments [37, 38]. Two types of machined cylindrical surfaces were made for the residual stress measurement. One was machined by fine turning followed by manual polishing using 1-μm diamond suspension, and another was by grinding, both being carried out in a commercial workshop. Figure 2 shows the morphology of the machined surfaces, which exhibit cutting-induced grooves indicative of surface plastic deformation. The TiN coating was deposited by a magnetron sputtering process on a pre-polished flat steel coupon of 30 mm in diameter.

The coating thickness is 2.69 μm as determined in previous research [9].

XRD experiments were carried out on an Empyrean X-ray diffractometer using a radiation of Co-K_α (wavelength 0.1789 nm, anode at 40 kV and 40 mA). For each cylindrical sample, measurements were made on the axial direction and the hoop direction, respectively. The height position of the surface to be measured was carefully calibrated to a precision of 0.002 mm using a dedicated micrometer. The incident X-ray beam was configured by a window of 15 mm in width and a ¼° incident slit. The diffractometer was configured at the Ω-2θ scan mode for scanning at 11 fixed Ω angles. Table 1 shows the design of Ω angles, in which the ferrite diffraction F(211) and the (220) diffraction of NaCl-type crystalline were selected in measuring the steel samples and the TiN coating sample, respectively. The Ω values were selected by considering the following factors.

1. The minimum Ω angle should be not less than 8°, since a low Ω angle was found to lead to an irregular diffraction peak for unknown reasons.
2. The selected Ω angles should lead to pairs of ±|ψ|, plus an Ω angle at approximately ψ=0, seeing Table 1.
3. The total number of Ω angles was determined after considering both the precision of linear regression and the experiment time.
4. The selected Ω angles should make an approximately uniform distribution of the sin²ψ values for the purpose of a fair linear regression.

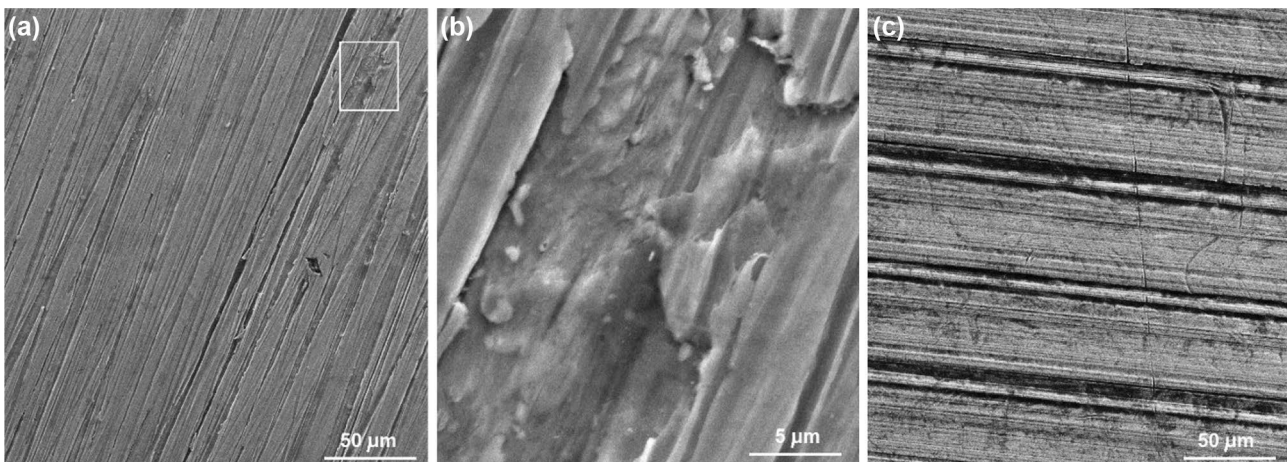


Fig. 2 Morphology of the machined surfaces observed by scanning electron microscopy: **a–b** the grinding finished surface; and **c** the turning machined surface. Note the cutting induced deformation and damages

Table 1 The designed settings of incident angle Ω , expected off-axis angle ψ and $\sin^2\psi$

Crystalline plane	No	1	2	3	4	5	6	7	8	9	10	11
F(112) of martensitic steel	Ω (°)	49.8	33.8	65.8	25.8	73.8	19.8	79.8	39.2	85.0	9.8	89.8
	ψ (°)	0.0	16.0	-16.0	24.0	-24.0	30.0	-30.0	35.2	-35.2	40.0	-40.0
	$\text{Sin}^2\psi$	0.00	0.08	0.08	0.17	0.17	0.25	0.25	0.33	0.33	0.41	0.41
(220) of TiN coating	Ω (°)	30.0	21.0	40.0	18.0	43.0	15.0	46.0	12.0	49.0	9.0	52.0
	ψ (°)	0.5	9.5	-9.5	12.5	-12.5	15.5	-15.5	18.5	-18.5	21.5	-21.5
	$\text{Sin}^2\psi$	0.00	0.03	0.03	0.05	0.05	0.07	0.07	0.10	0.10	0.13	0.13

In all the X-ray acquisition, a small step size 0.053° and a slow scanning speed 0.004° per second were applied to obtain sufficiently high peak intensity. Given the applied diffraction conditions and linear absorption coefficient of $K_\alpha\text{-Co}$ in iron ($\mu/\rho = 59.5 \text{ cm}^2/\text{g}$), the resultant X-ray depth penetration to the machined steel surfaces was between 3.1 and $8.1 \mu\text{m}$. All the acquired diffraction data were processed by $K_{\alpha 2}$ stripping and substrate removing, and then further filtered by Lorentz-Polarization-Absorption before the diffraction peak measurement. The diffraction peaks were measured using the parabolic approach, which was recommended from our previous work to show the minimum deviation [6]. In the stress calculation, the E modulus and Poisson's ratio ν of the steel were adapted as 210 GPa and 0.30 , respectively, whereas the E modulus and Poisson's ratio ν of the TiN coating were adapted as 300 GPa and 0.23 , respectively [6, 9, 33].

4 Results and discussion

4.1 XRD measurements and related linear regressions

Figure 3 shows the results of XRD residual measurements at the axial direction of the turning machined sample, including both the conventional $d \sim \sin^2\psi$ method and the new $\sin^2\psi\text{-sin}(2\psi)$ method. The diffraction curves obtained at the pre-defined Ω angles are summarised in Fig. 3a. Figure 3b shows the diffraction peak angles 2θ plotted versus the corresponding ψ angles. Figure 3c shows two linear regressions by processing the obtained 2θ and ψ data following Eqs. (6) and (10), respectively. Figure 3c reveals good linear relationship between $\frac{d_\psi + d_{-\psi}}{2}$ and $\sin^2\psi$. A pronounced splitting exists in the $d \sim \sin^2\psi$ series, indicating different $d \sim \sin^2\psi$ variations for the positive and negative ψ angles. The linear regression $\frac{d_\psi + d_{-\psi}}{2} \sim \sin^2\psi$ turns out a high precision factor of $R^2 = 0.999$. As compared to the

precision factor $R^2 = 0.833$ of the conventional regression $d \sim \sin^2\psi$, the significantly increased R^2 value suggests a more accurate measurement. Figure 3d shows the linear regression between $(d_\psi - d_{-\psi})$ and $\sin(2\psi)$, as suggested by Eq. (13).

The results of the calculation are summarised in Table 2. For the conventional $d \sim \sin^2\psi$ method, linear regressions using the positive and negative ψ angles turn out different residual compressive stress values, namely, of $-585.7 \pm 24.7 \text{ MPa}$ and $-995.0 \pm 12.7 \text{ MPa}$, respectively. The overall $d \sim \sin^2\psi$ linear regression, from all the positive and negative ψ angles, turns out a residual normal stress of $-787.3 \pm 117.7 \text{ MPa}$, noticing the significant deviation. In contrast, the residual normal stress determined from the new $\sin^2\psi\text{-sin}(2\psi)$ method is $-778.0 \pm 10.6 \text{ MPa}$, having greatly decreased deviation. Meanwhile, a residual shear stress of $157.2 \pm 30.7 \text{ MPa}$ has been determined. The results, including both the residual stress values and the associated deviation, are illustrated in Fig. 4, which clearly reveal the advantages of the new $\sin^2\psi\text{-sin}(2\psi)$ method both in the greatly decreased deviation in the measured residual normal stress and in the feasibility in residual shear stress measurement. In particular, the $d \sim \sin^2\psi$ splitting suggests the co-existence of a residual shear stress.

Figures 5, 6, 7 and 8 show the measurements of other samples. Similarly, these measurements all reveal high precision (R^2) of the new linear regressions, ranging from 0.871 (Fig. 5c) to 0.987 (Fig. 8c), suggesting consistently increased accuracy of the new method as compared to the conventional method. Meanwhile, the $(d_\psi - d_{-\psi}) \sim \sin 2\psi$ regressions also reveal high values of precision factor R^2 , ranging from 0.877 (Fig. 5d) to 0.962 (Figs. 6d and 8d), suggesting consistently the feasibility of residual shear stress measurements. In contrast, the R^2 values of the conventional $d \sim \sin^2\psi$ regressions are much lower, ranging from 0.153 (Fig. 7c) to 0.856 (Fig. 8c). These results indicate superior performance of the new method to the conventional method.

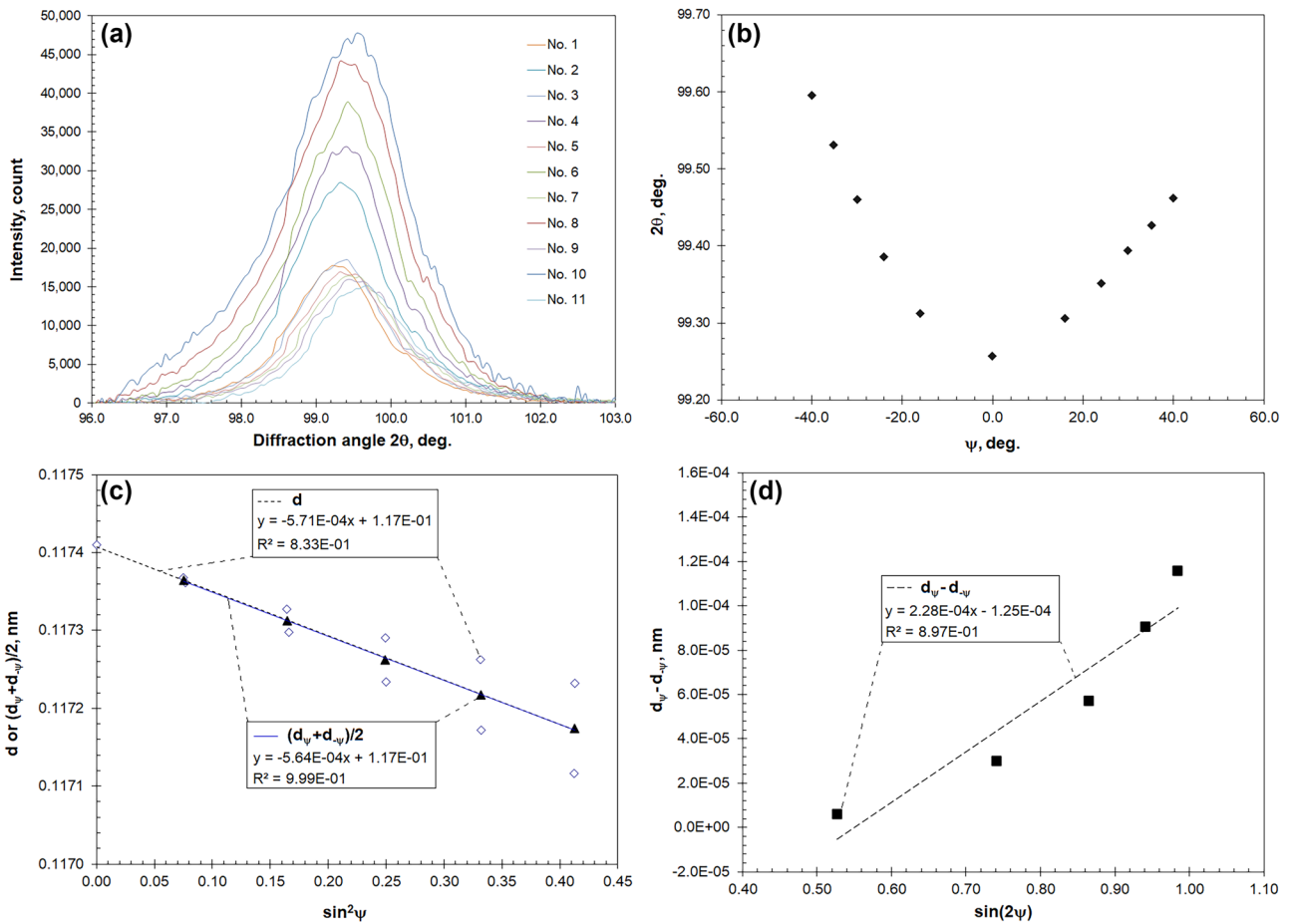


Fig. 3 Residual stress measurement at the axial direction of the turning machined cylindrical sample: **a** A collection of the diffraction peaks; **b** Plot of the measured diffraction angle 2θ versus the off-axis

angle ψ ; **c** Linear regression plots $d \sim \sin^2\psi$ and $\frac{d_\psi + d_{-\psi}}{2} \sim \sin^2\psi$; and **d** Linear regression plot $(d_\psi - d_{-\psi}) \sim \sin(2\psi)$

4.2 Residual normal stresses determined using the new method and conventional method

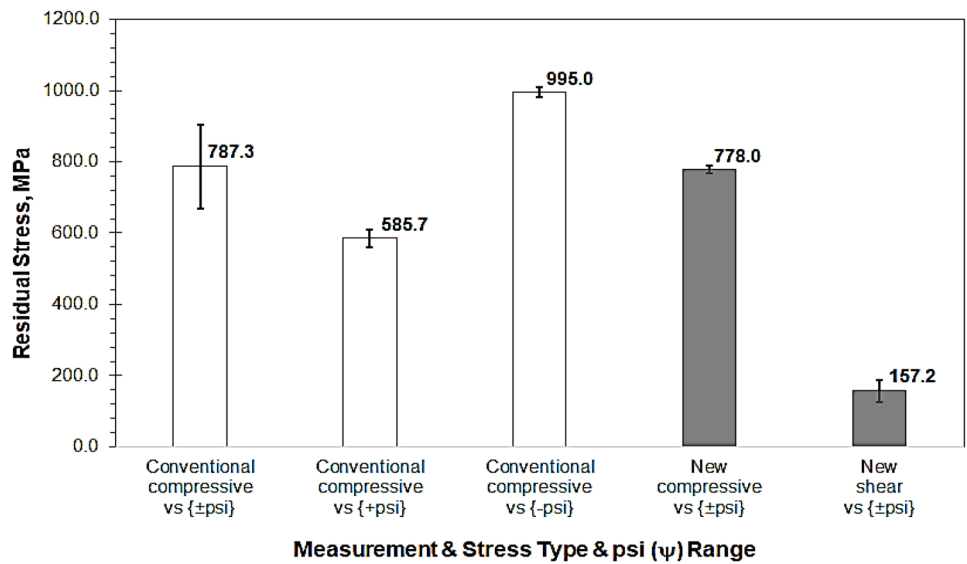
The results of calculated residual normal stresses and strain-free d-spacings are summarised in Table 3. Comparing to the conventional method, the new method proposed in this paper is able to provide more accurate measurement of residual stresses.

Both the conventional method and the new method turn out similar values of normal residual stress. For example, the turning machined steel showed residual normal stresses at both the axial and hoop directions, whereas the values determined by the two methods are comparable to each other, e.g., -787.3 MPa and -778.0 MPa at the axial direction as determined by the conventional and new methods,

Table 2 The results of residual axial stress calculation of the turning machined sample

Method	Stress	Regression $Y = A \cdot X + B$, precision R^2			Stress, MPa		d_0 , nm
		A	B	R^2	Value	Deviation	
Traditional method	σ vs $\{\pm \psi\}$	$-5.71E-04$	$1.17E-01$	83.3%	-787.3	-117.7	0.1172
	σ vs $\{+\psi\}$	$-4.25E-04$	$1.17E-01$	99.3%	-585.7	24.7	0.1172
	σ vs $\{-\psi\}$	$-7.21E-04$	$1.17E-01$	99.9%	-995.0	12.7	0.1171
New method	σ	$-5.64E-04$	$1.17E-01$	99.9%	-778.0	10.6	0.1172
	τ	$2.28E-04$	$-1.25E-04$	89.7%	-157.2	30.7	

Fig. 4 Comparison of residual normal and shear stresses, values and deviation, measured using the conventional and new methods



respectively. Such residual stresses could be attributed predominantly to the fast straining in the applied turning [17]. Several cutting parameters, including cutting speed, feed

rate, cutting depth, tool wear, and the use of lubricant, have strong influence on the residual stress formation [16, 17, 21].

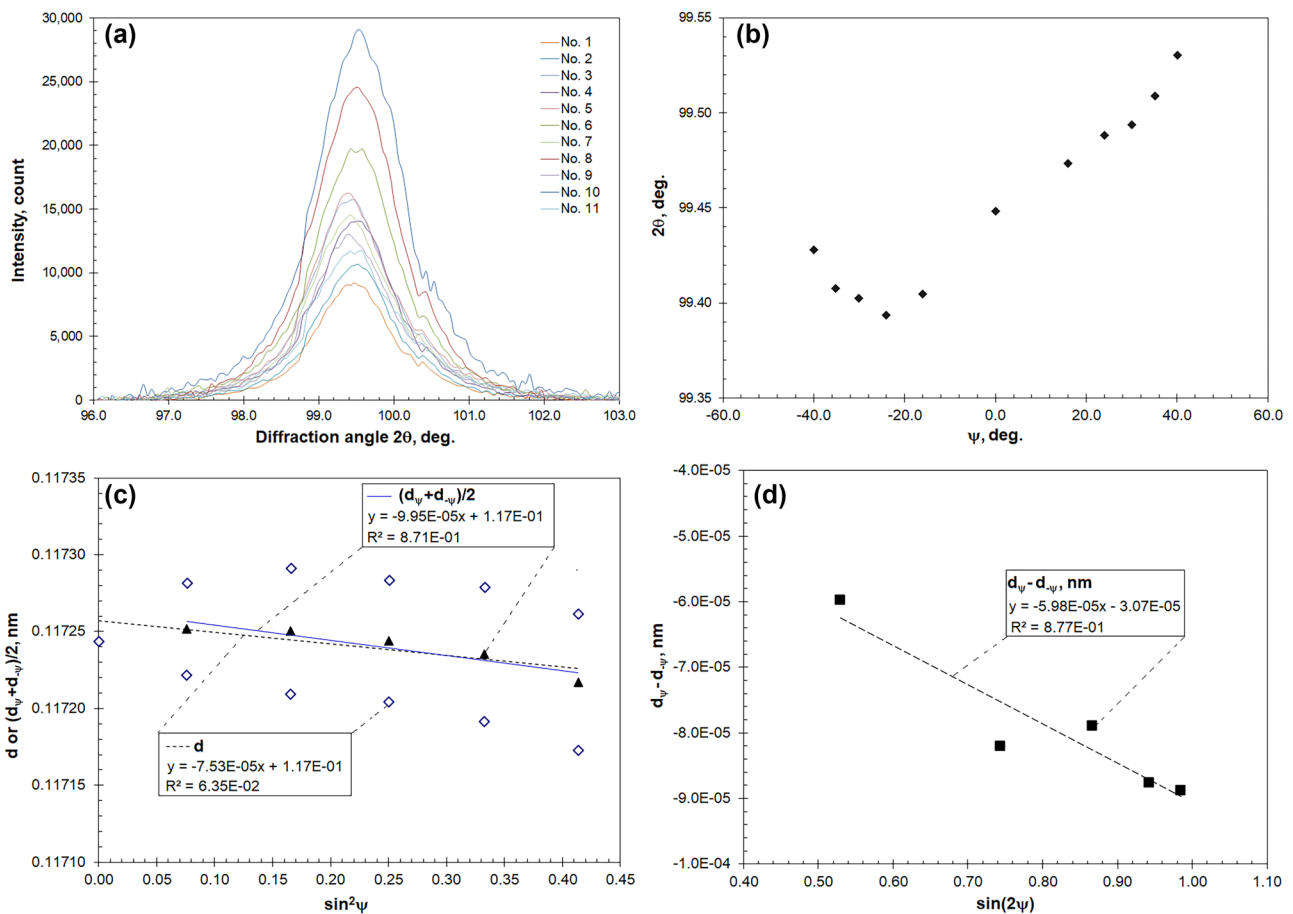


Fig. 5 Residual stress measurement at the hoop direction of the turning machined cylindrical bar: **a** The obtained diffraction peaks; **b** The measured diffraction angle 2θ plotted versus the off-axis angle ψ ; **c**

Linear regression plots $d_\psi \sim \sin^2\psi$ and $\frac{d_\psi + d_{-\psi}}{2} \sim \sin^2\psi$, and **d** Linear regression plot $(d_\psi - d_{-\psi}) \sim \sin(2\psi)$

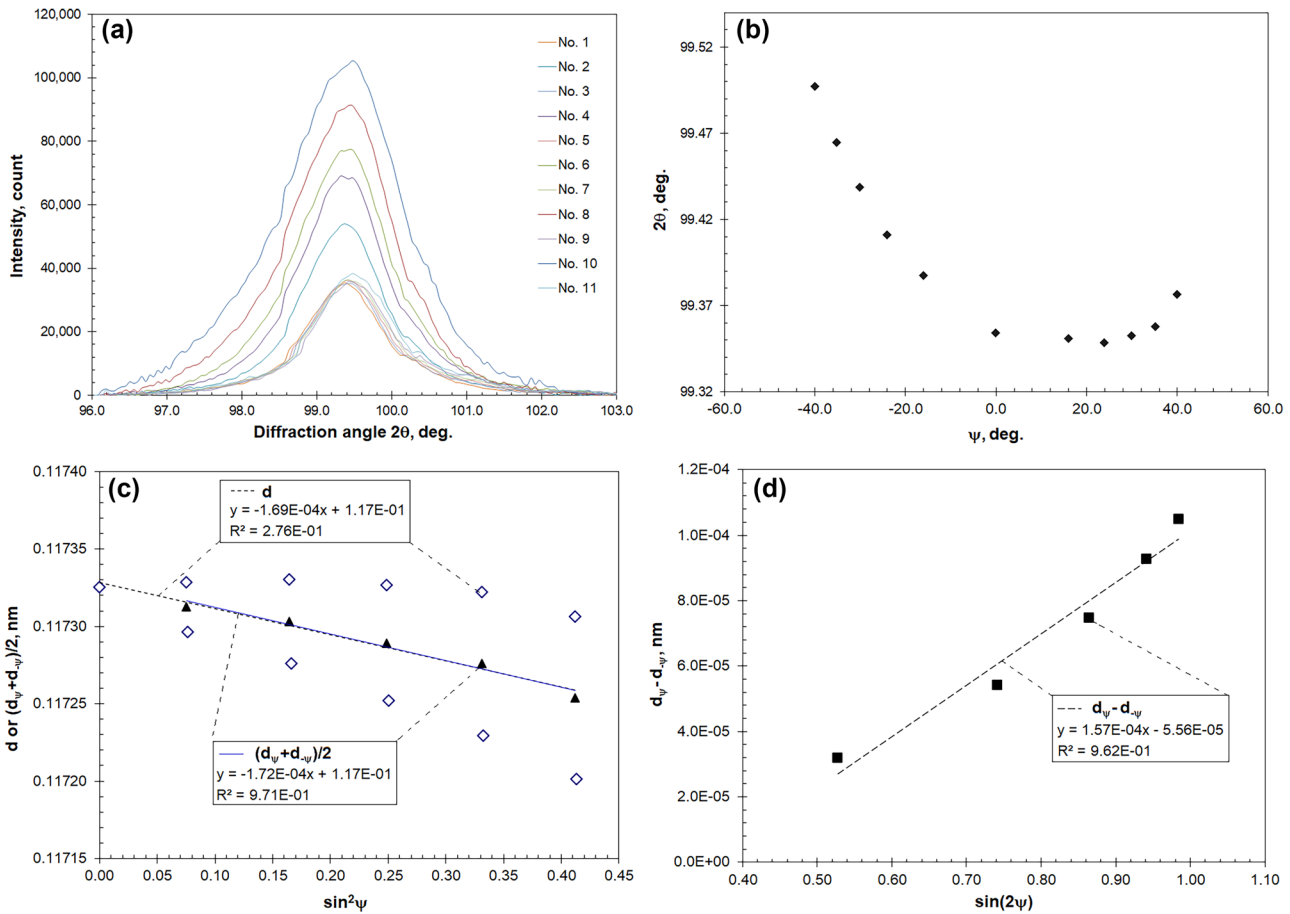


Fig. 6 Residual stress measurement at the axial direction of the ground cylindrical bar: **a** A collection of the diffraction peaks; **b** Plot of the measured diffraction angle 2θ versus the off-axis angle ψ ; **c**

Linear regression plots $d_\psi \sim \sin^2\psi$ and $\frac{d_\psi + d_{-\psi}}{2} \sim \sin^2\psi$; and **d** Linear regression plot $(d_\psi - d_{-\psi}) \sim \sin(2\psi)$

For linear regression, the precision factor R^2 provides a measurement of scattering or uncertainty. The R^2 values of the linear regression treatments in Figs. 3, 5, 6, 7 and 8 are summarised in Fig. 9. The conventional method shows R^2 values from 0.06 to 0.86, in which three of the five values are less than 0.30, suggestive of large uncertainty in the stress measurement. The deviation relates directly to the scale of the $\sin^2\psi$ splitting, e.g., seeing Figs. 3c and 5c for the turning machined sample. On the other hand, the new method provides a reliable solution to the $\sin^2\psi$ splitting. The R^2 values for both the normal stress and shear stress measurements are consistently higher than 0.85. Obviously, the new method is able to perform residual stress measurement at significantly increased precision. The R^2 values of the shear stress measurements are slightly inferior to the relevant values of the normal stress measurements. Nevertheless, the new method has made it possible to

determine both the residual normal and shear stresses simultaneously using the XRD Ω - 2θ configuration.

The grinding machined sample also showed residual compressive stresses in both the axial and hoop directions. Again, the new method shows advantage in the substantially reduced deviation, e.g., from 137.6 to 22.4 MPa in the measurements at the axial direction. It is not the scope of this paper to compare the scales of residual stresses generated in the two different machining operations or to investigate the effect of machining parameters on the residual stresses. However, the precise measurement of machining-induced residual stresses provided a strong support to the research and development of the ultrahigh strength steel [37, 38]. The optimised machining process helped to minimise the residual stresses of the turning- and grinding-machined specimens, which contributed to reliable measurements of mechanical properties in tensile and fatigue tests.

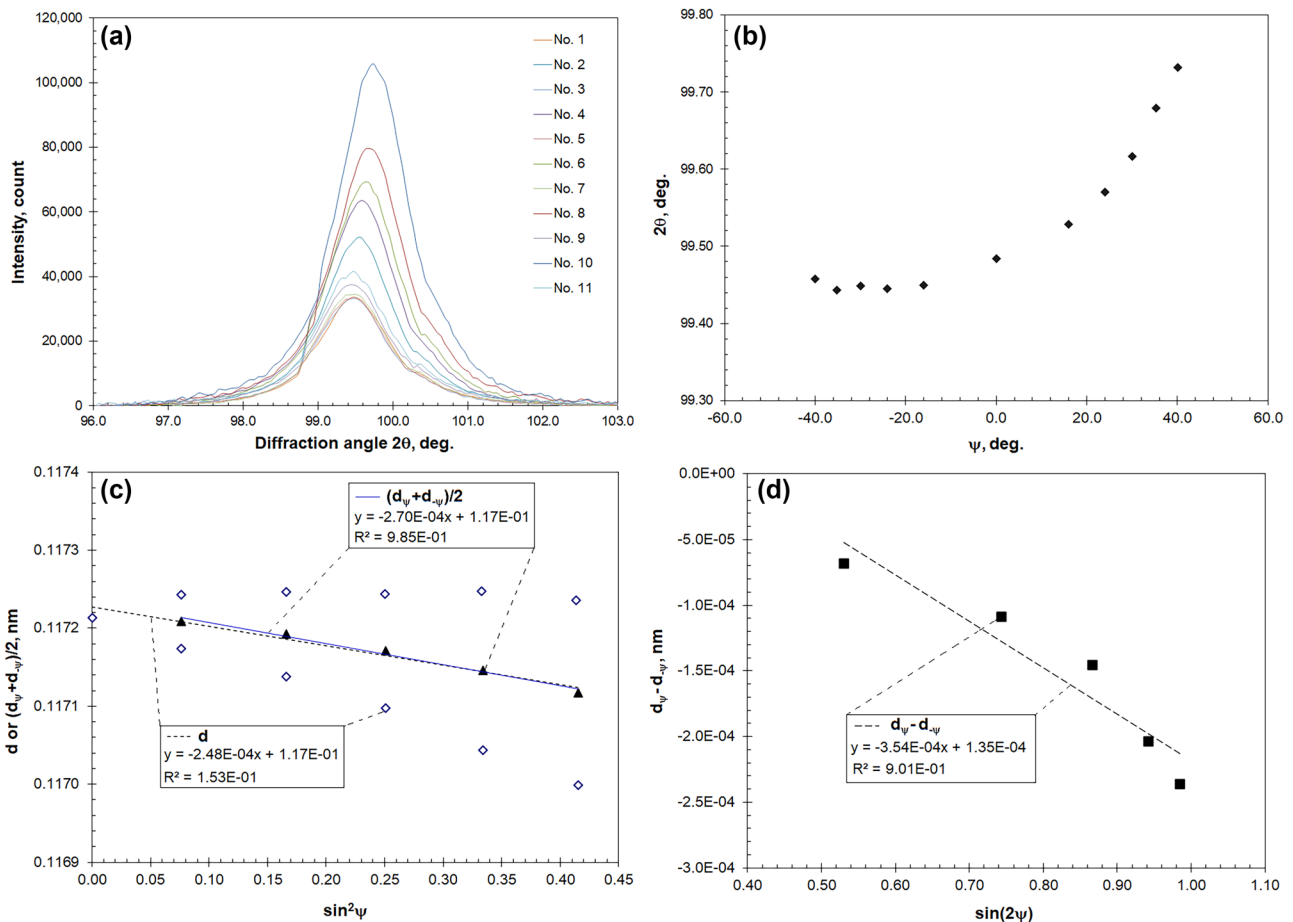


Fig. 7 Residual stress measurement at the hoop direction of the ground cylindrical bar: **a** A collection of the diffraction peaks; **b** Plot of the measured diffraction angle 2θ versus the off-axis angle ψ ;

c Linear regression plots $d_\psi \sim \sin^2\psi$ and $\frac{d_\psi + d_{-\psi}}{2} \sim \sin^2\psi$; and **d** Linear regression plot $(d_\psi - d_{-\psi}) \sim \sin(2\psi)$

4.3 Residual shear stresses determined by the new method

The new method provides a reliable measurement of the residual shear stress. Table 3 suggests co-existence of residual shear stresses and normal stresses in all the machined surfaces, having the ratio $\tau_{13}:\sigma_1$ ranging from 1:5 to 1:1.5. In particular, the minimum ratio 1:1.5 indicates substantially high residual shear stress. On the other hand, the TiN coating indicates an extremely low $\tau_{13}:\sigma_1$ ratio of 1:31.3. This result matches well to the expectation that sputtered coatings are known to have only residual normal stresses because of the thin film growth modes [1, 5, 10]. This can be considered as a verification to the measurement of residual shear stress.

In Table 3, the scale of shear stress depends directly on the $\sin^2\psi$ splitting. The samples having large residual shear stresses show remarkable $\sin^2\psi$ splitting, whereas those having low shear stresses show marginal $\sin^2\psi$ splitting. The presence of residual shear stresses agrees to literature [8, 20, 22, 24, 25]. The XRD measurement of residual shear stresses used to be more complicated than the measurement of residual normal stresses, whereas the former may involve different instrumental configurations, multi-axial measurement and massive data processing [11, 12, 20, 22–24]. Comparing to those methods reported in the literature, the new $(d_\psi - d_{-\psi}) \sim \sin(2\psi)$ method is straightforward for it is developed from the mostly used $d \sim \sin^2\psi$ method, which therefore can be undertaken under the same instrumental configuration.

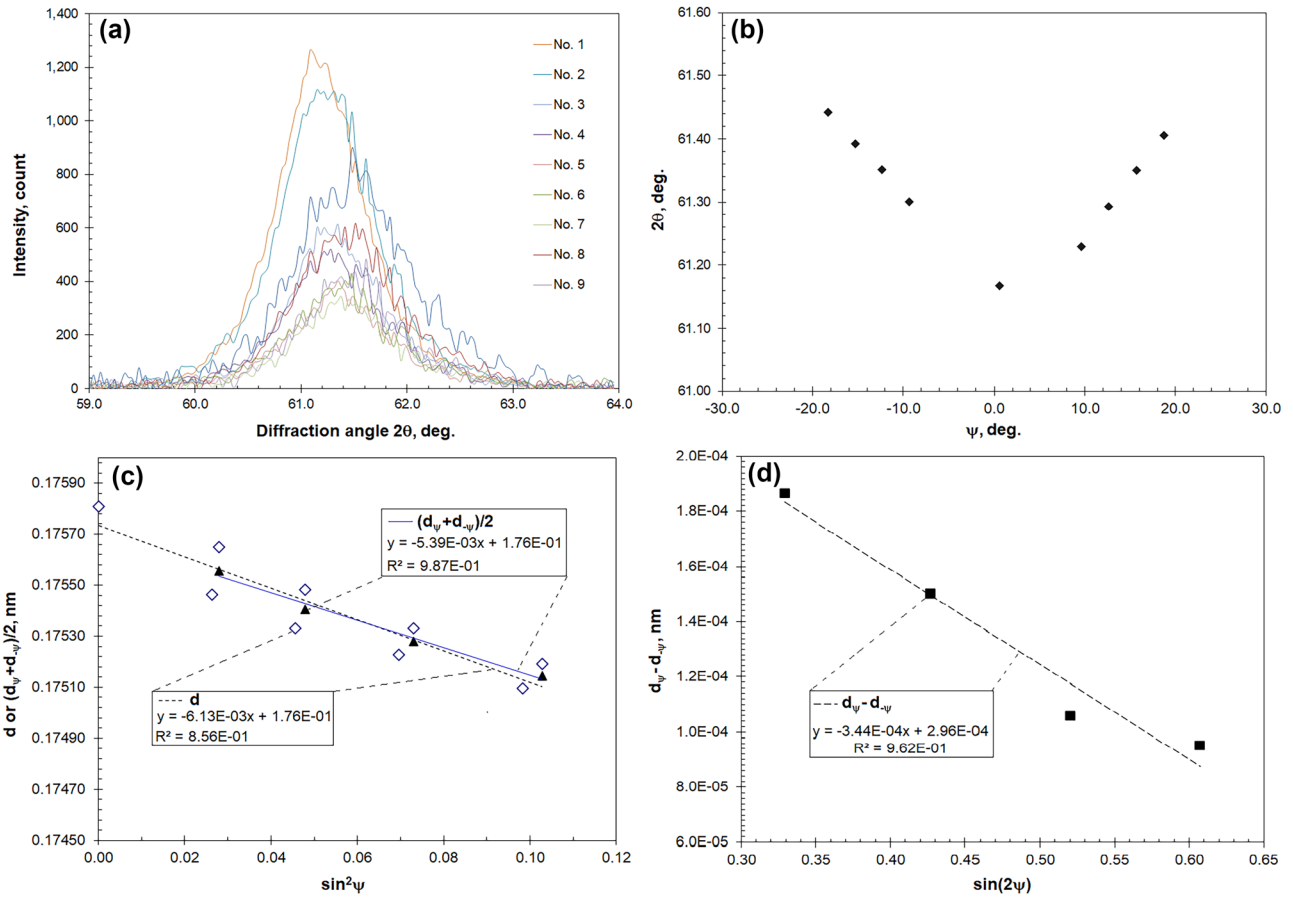
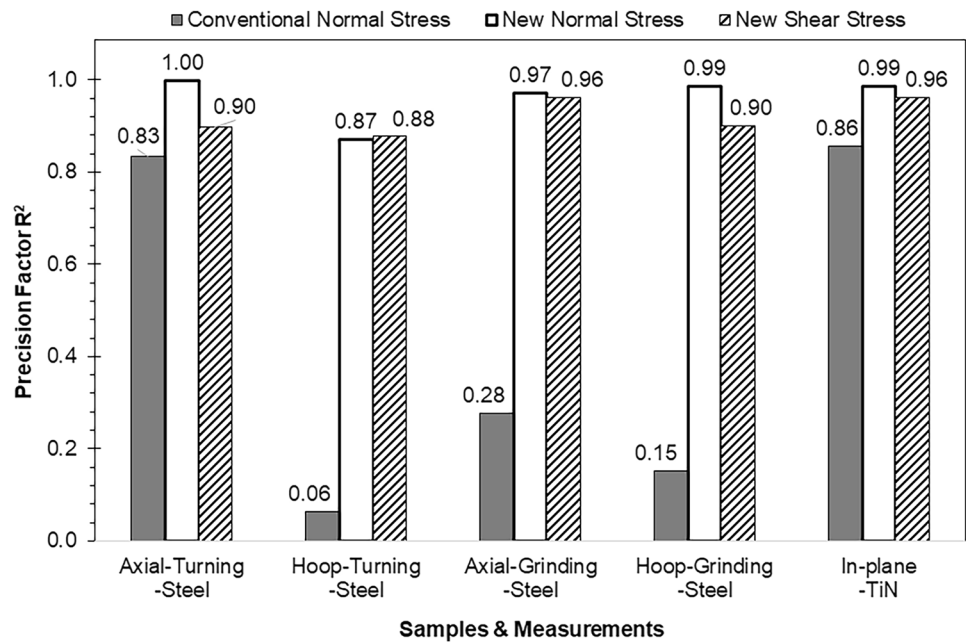


Fig. 8 Residual stress measurement of a magnetron sputtered TiN coating: **a** A collection of the diffraction peaks; **b** Plot of the measured diffraction angle 2θ versus the off-axis angle ψ ; **c** Linear regression plots $d_{\psi} \sim \sin^2\psi$ and $\frac{d_{\psi} + d_{-\psi}}{2} \sim \sin^2\psi$; and **d** Linear regression plot $(d_{\psi} - d_{-\psi}) \sim \sin(2\psi)$

Table 3 Summary of residual stresses (σ_1 and τ_{13}) and strain-free d-spacing (d_0)

Sample	Conventional		$(d_{\psi} + d_{-\psi})/2 \sim \sin^2\psi$; $d \sim \sin^2\psi$			$\tau_{13}:\sigma_1$	
	σ_1 (MPa)	d_0 (nm)	σ_1 (MPa)	d_0 (nm)	τ_{13} (MPa)		
Turning	Axial	-787.3 ± 117.7	0.1171	-778.0 ± 10.6	0.1172	157.2 ± 30.7	1:5.0
	Hoop	-103.8 ± 132.9	0.1172	-137.2 ± 30.5	0.1172	41.2 ± 8.9	1:3.3
Grinding	Axial	-252.8 ± 137.6	0.1173	-256.3 ± 22.4	0.1173	103.5 ± 9.0	1:2.5
	Hoop	-342.5 ± 269.2	0.1171	-372.3 ± 26.5	0.1171	244.0 ± 46.8	1:1.5
TiN coating		-8623 ± 1354	0.1734	-7564 ± 613	0.1737	242 ± 34	1:31.3

Fig. 9 Comparison of the precision factor R^2 obtained using the conventional and new methods



5 Conclusions

A new $\sin^2\psi$ - $\sin(2\psi)$ method has been developed for simultaneous measurement of both residual normal and shear stresses. The new method derives from modification of the conventional $d \sim \sin^2\psi$ method, with the following recommended procedure.

1. Select a lattice plane of a polycrystalline sample to perform an XRD scan under the θ - 2θ mode and measure its diffraction angle $2\theta_0$.
2. Design a series of off-axis angle $\pm\psi$ ($\psi > 0$) and calculate the corresponding incident angle Ω of every ψ angle using the equation $\Omega = \theta_0 - \psi$.
3. Perform an XRD scan at every calculated incident angle Ω under the Ω - 2θ mode and measure the position 2θ of every obtained diffraction peak.
4. Calculate the d-spacing d_ψ and ψ for every obtained 2θ angle by using the Bragg law and the equation $\psi = \theta - \Omega$, respectively.
5. Perform linear regressions using Eqs. (9) and (12), to calculate the residual normal and shear stresses, respectively.

The new method has been verified on two cylindrical steel bars produced by turning and grinding, respectively, as well as a TiN coating grown on stainless steel by magnetron sputtering deposition. Both the turning- and grinding-machined bars showed residual normal and shear stresses having various ratios between the normal and shear stresses.

The TiN coating showed high scale of residual compressive (normal) stress whereas the residual shear stress was relatively marginal. In measuring residual normal stresses, the new method showed significantly improved precision as compared to the conventional $d \sim \sin^2\psi$ method.

Author contribution As the single author, Q. Luo contributed to the theoretical development, the design and conduction of experiments, and the manuscript writing up.

Availability of data and material All related data and materials are as described in the paper.

Declarations

Ethics approval and consent to participate Not applicable.

Consent for publication Not applicable.

Conflict of interest The author declares no competing interests.

Open Access This article is licensed under a Creative Commons Attribution 4.0 International License, which permits use, sharing, adaptation, distribution and reproduction in any medium or format, as long as you give appropriate credit to the original author(s) and the source, provide a link to the Creative Commons licence, and indicate if changes were made. The images or other third party material in this article are included in the article's Creative Commons licence, unless indicated otherwise in a credit line to the material. If material is not included in the article's Creative Commons licence and your intended use is not permitted by statutory regulation or exceeds the permitted use, you will need to obtain permission directly from the copyright holder. To view a copy of this licence, visit <http://creativecommons.org/licenses/by/4.0/>.

References

1. Teixeira V, Andritschky M, Fischer W, Buchkremer HP, Stover D (1999) Effects of deposition temperature and thermal cycling on residual stress state in zirconia-based thermal barrier coatings. *Surf Coat Technol* 120–121:103–111
2. Murotani T, Hirose H, Sasaki T, Okazaki K (2000) Study on stress measurement of PVD-coating layer. *Thin Solid Films* 377:617–620
3. Cullity BD, Stock SR (2001) *Elements of x-ray diffraction*, 3rd edn. Prentice Hall, Upper Saddle River, NJ, p p435
4. Welzel U, Ligot J, Lamparter P, Vermeulen AC, Mittemeijer EJ (2005) Stress analysis of polycrystalline thin films and surface regions by X-ray diffraction. *J Appl Crystall* 38:1–29
5. Moreno CM, Sanchez JM, Ardila LC, Aldareguia JMM (2009) Determination of residual stresses in cathodic arc coatings by means of the parallel beam glancing X-ray diffraction technique. *Thin Solid Films* 518:206–222
6. Luo Q, Jones AH (2010) High-precision determination of residual stress of polycrystalline coatings using optimised XRD- $\sin^2\psi$ technique. *Surf Coat Technol* 205:1403–1408
7. Luo Q, Yang S (2017) Uncertainty of the X-ray diffraction (XRD) $\sin^2\psi$ technique in measuring residual stresses of physical vapor deposition (PVD) hard coatings. *Coatings* 7:128
8. Meixner M, Klaus M, Zinn W, Apel D, Liehr A, Genzel C, Scholtes B (2018) Analysis of multiaxial near-surface residual stress fields by energy- and angle-dispersive X-ray diffraction: semi-versus non-destructive techniques. *Mater Perform Character* 7:465–487
9. Luo Q, Yang S, Cooke KE (2013) Hybrid HIPIMS and CFUBMS deposition of TiN coatings: deposition rate, structure and tribological properties. *Surf Coat Technol* 236(2013):13–21
10. Liu H, Xu Q, Zhang X, Wang C, Tang B (2013) Residual stress analysis of TiN film fabricated by plasma immersion ion implantation and deposition process. *Nucl Instrum Method Phys Res B* 297:1–6
11. Pineault JA, Belassel M, Brauss ME (2002) X-ray diffraction residual stress measurement in failure analysis, in *ASM Handbook, Vol. 11: Failure analysis and prevention*, ed. Becker WT, Shipley RJ. ASM Int 484–497
12. Pala Z, Ganev N (2010) The impact of various cooling environments on the distribution of macroscopic residual stresses in near-surface layers of ground steels. *Mater Sci Eng* 497A:200–205
13. Xin M, Xie L, Wang X, Run S, Yang H (2010) Study on the surface residual stress of high hardness and strength alloy steel in high speed milling. *Trans Beijing Instit Technol* 30:19–23
14. Zhang VH, Zhang X, Zhang H, Ren Y, Liu G (2016) Surface quality of high-speed turning 300M ultrahigh strength steel. *Surf Technol* 45:181–187
15. Liu J, Hou D (2008) Study on residual stress in grinding-hardened layer of 40Cr steel. *Heat Treat Met* 33:127–130
16. Madariaga A, Kortabarria A, Hormaetxe E, Garay A, Arrazola PJ (2016) Influence of tool wear on residual stresses when turning Inconel 718. *Procedia CIRP* 45:267–270
17. Jang DY, Watkins TR, Kozaczek KJ, Hubard CR, Cavin OB (1999) Surface residual stresses in machined austenitic stainless steel. *Wear* 194:168–173
18. Balart MJ, Bouzina A, Edwards L, Fitzpatrick ME (2004) The onset of tensile residual stresses in grinding of hardened steels. *Mater Sci Eng* 367A:132–142
19. Ding W, Zhang L, Li Z, Zhu Y, Su H, Xu J (2017) Review on grinding induced residual stresses in metallic materials. *Int J Adv Manuf Technol* 88:2939–2968
20. Hua Y, Liu Z (2019) Effects of machining induced residual shear and normal stresses on fatigue life and stress intensity factor of Inconel 718. *Appl Sci* 9:4750
21. Wang SQ, Li JG, He CL, Laghari RA (2019) An analytical model of residual stress in orthogonal cutting based on the radial return method. *J Mater Process Technol* 273:116234.
22. Perenda J, Trajkovski J, Zerovnik A, Prebil I (2016) Modelling and experimental validation of the surface residual stresses induced by deep rolling and presetting of a torsion bar. *Int J Mater Form* 9:435–448
23. Tanaka K (2017) The $\cos\alpha$ method for X-ray residual stress measurement using two-dimensional detector. *Mech Eng Rev* 6:18–00378
24. Zauskova L, Czana A, Sajgalik M, Drbul M, Rysava Z (2017) Triaxial measurement of residual stress after high feed milling using X-ray diffraction. *Proced Eng* 192:982–987
25. Huang XD, Zhang XM, Ding H (2016) A novel relaxation-free analytical method for prediction of residual stress induced by mechanical load during orthogonal machining. *Int J Mech Sci* 115–116:299–309
26. Kikuchi S, Nakamura Y, Nambu K, Ando M (2015) Effect of shot peening using ultra-fine particles on fatigue properties of 5056 aluminium alloy under rotating bending. *Mater Sci Eng* 652:279–286
27. Nalla RK, Altenberger I, Noster U, Liu GY, Scholtes B, Ritchie RO (2003) On the influence of mechanical surface treatments — deep rolling and laser shock peening — on the fatigue behaviour of Ti-6Al-4V at ambient and elevated temperatures. *Mater Sci Eng* 355A:216–230
28. Kim JC, Cheong SK, Noguchi H (2013) Residual stress relaxation and low-and high-cycle fatigue behaviour of shot-peened medium-carbon steel. *Int J Fatigue* 56:114–122
29. Tang LQ, Qian CF, Ince A, Zheng J, Li HF, Han ZC (2018) Fatigue crack growth behaviour of the MIG welded joint of 06Cr19Ni20 stainless steel. *Materials* 11:1336
30. Leggett RH (2008) Residual stresses in welded structures. *Int J Press Vessel Pip* 85:144–151
31. Harjo S, Tomota Y, Ono M (1998) Measurements of thermal residual elastic strains in ferrite-austenite Fe-Cr-Ni alloys by neutron and X-ray diffractions. *Acta Mater* 47:353–362
32. Sinha VK, Godaba VS (2008) Residual stress measurement in worked and heat treated steel by X-ray diffractometry. *Mater Sci Eng* 488A:491–495
33. Navas VG, Gonzalo O, Quintana I, Pirling T (2011) Residual stresses and structural changes generated at different steps of the manufacturing of gears: effect of banded structures. *Mater Sci Eng* 528A:5146–5157
34. Ghosh S, Rana VPS, Kain V, Mittal V, Baveja SK (2011) Role of residual stresses induced by industrial fabrication on stress corrosion cracking susceptibility of austenitic stainless steel. *Mater Design* 32:3823–3831
35. Zhang W, Fang K, Hu Y, Wang S, Wang X (2016) Effect of machining-induced surface residual stress on initiation of stress corrosion cracking in 316 austenitic stainless steel. *Corros Sci* 108:173–184
36. Matsuda M, Okita K, Nakagawa T, Sasaki T (2017) Application of X-ray stress measurement for residual stress analysis by inherent strain method — comparison of $\cos\alpha$ and $\sin^2\psi$ method. *Mech Eng J* 4:17–00022
37. Luo Q, Kitchen M, Patel V, Filleul M, Owens D (2016) Partial-isothermally-treated low alloy ultrahigh strength steel with martensitic/bainitic microstructure. *Proceedings HSLA Steels* 2015:433–438
38. Luo Q, Kitchen M, Abubakri S (2017) Effect of austempering time on the microstructure and carbon partitioning of ultrahigh strength steel 56NiCrMoV7. *Metals* 7:258

Publisher's Note Springer Nature remains neutral with regard to jurisdictional claims in published maps and institutional affiliations.